Anisotropic charge density wave in layered $1T$-$TiSe_2$

Qiao Qiao,[1,2] Songsong Zhou,[3] Jing Tao,[2] Jin-Cheng Zheng,[4] Lijun Wu,[2] Samuel T. Ciocys,[5] Maria Iavarone,[1] David J. Srolovitz,[3,6] Goran Karapetrov,[5] and Yimei Zhu[2,*]

[1]*Department of Physics, Temple University, Philadelphia, Pennsylvania 19122, USA*

[2]*Condensed Matter Physics and Materials Science Department, Brookhaven National Laboratory, Upton, New York 11973, USA*

[3]*Department of Materials Science and Engineering, University of Pennsylvania, Philadelphia, Pennsylvania 19104, USA*

[4]*Department of Physics, and Collaborative Innovation Center for Optoelectronic Semiconductors and Efficient Devices, Xiamen University, Xiamen, Fujian 361005, China*

[5]*Department of Physics, Drexel University, Philadelphia, Pennsylvania 19104, USA*

[6]*Department of Mechanical Engineering and Applied Mechanics, University of Pennsylvania, Philadelphia, Pennsylvania 19104, USA*

(Received 6 April 2017; published 4 October 2017)

We present a three-dimensional study on the anisotropy of the charge density wave (CDW) in $1T$-$TiSe_2$, by means of *in situ* atomically resolved electron microscopy at cryogenic temperatures in both reciprocal and real spaces. Using coherent nanoelectron diffraction, we observed short-range coherence of the in-plane CDW component while the long-range coherence of out-of-plane CDW component remains intact. An in-plane CDW coherence length of ∼10 nm and an out-of-plane CDW coherence length of 17.5 nm, as a lower bound, were determined. The electron modulation was observed using electron energy-loss spectroscopy and verified by an orbital-projected density of states. Our integrated approach reveals anisotropic CDW domains at the nanoscale, and illustrates electron modulation-induced symmetry breaking of a two-dimensional material in three dimensions, offering an opportunity to study the effect of reduced dimensionality in strongly correlated systems.

DOI: 10.1103/PhysRevMaterials.1.054002

I. INTRODUCTION

Modulations of electrons, phonons, and spins render symmetry breaking in strongly correlated materials. From a delicate balance of their interactions arise unconventional macroscopic phenomena such as high-T_c superconductivity and colossal magnetoresistance. Particularly, material systems containing charge density waves (CDWs) are ideal for studying structural symmetry breaking induced by electron modulation, serving as a step toward a better understanding of the intricate quantum phenomena that stem from electron-phonon coupling and electron-electron interactions. $1T$-$TiSe_2$ is a quasi-two-dimensional semimetal exhibiting strongly correlated electron behavior. It undergoes a phase transition at ∼200 K, transforming into a commensurate CDW state. The periodic lattice distortion (PLD) expands the unit cell into a $2 \times 2 \times 2$ superlattice. Studies on the origin of the CDW phase transition in $1T$-$TiSe_2$ have been actively conducted for decades. The Fermi surface nesting model [1] has been proven to be improbable by experimental results showing anisotropic electron and hole pockets [2]. Instead, models based on electron-electron interactions (excitonic insulator) [3–5] and electron-phonon coupling (band Jahn-Teller effect) [6–8] have been proposed for $1T$-$TiSe_2$. To date, a quantitative theory on the origin of CDW in $1T$-$TiSe_2$ is still lacking, but based on experiments conducted using terahertz spectroscopy, time-resolved angle-resolved photoemission spectroscopy (ARPES), and momentum-resolved electron energy-loss spectroscopy (EELS), agreement has been reached that both electron-phonon coupling and electron-electron interactions play an important role [9–11].

The $1T$-$TiSe_2$ system is of particular interest since it not only exhibits CDW phase transitions, but can also be superconducting. Superconductivity is found in pure $1T$-$TiSe_2$ under pressure [12], and has been found to be strongly connected to the formation of CDW domain walls [13]. On the other hand, the Cava group reported that upon Cu intercalation, the CDW transition is suppressed and superconductivity emerges [14]. According to the BCS theory, electron-phonon coupling could drive the formation of electron pairs that leads to conventional superconductivity. At the CDW phase transition temperature, Weber *et al.* observed a complete softening of a transverse optic phonon at the L point, which indicates that strong electron-phonon coupling also plays a role in stabilizing the CDW/PLD, which aligns with the band Jahn-Teller effect theorem [7,15]. So far, a number of experimental investigations have been performed to study the CDW phase transition in $1T$-$TiSe_2$. However, due to the limitation of experimental techniques related to the low-dimensional nature of the material, research has been confined either to the top surface of the material [16–18], or purely in reciprocal space that measures averaged properties without spatial resolution [4,19–23]. A full-scale study in all three dimensions of real space combined with reciprocal space information is yet to be conducted, limiting the ability to correlate the bulk property, and the underlying non-two-dimensional structure of the CDW domain.

In this paper, we solve this dilemma by integrating a set of experimental approaches using transmission electron microscopy. We use coherent nanoarea electron diffraction (NED) to unravel three-dimensional reciprocal space properties; we acquire position-averaged convergent beam electron diffraction (PACBED) to reveal the real space nanometer scale domain distribution with depth information; we collect atomic-resolution scanning transmission electron microscopy (STEM) and EELS to access both real space and the energy space information. Our results show that the CDW forms three-dimensional cylindrically shaped domains, with different

*Corresponding author: zhu@bnl.gov

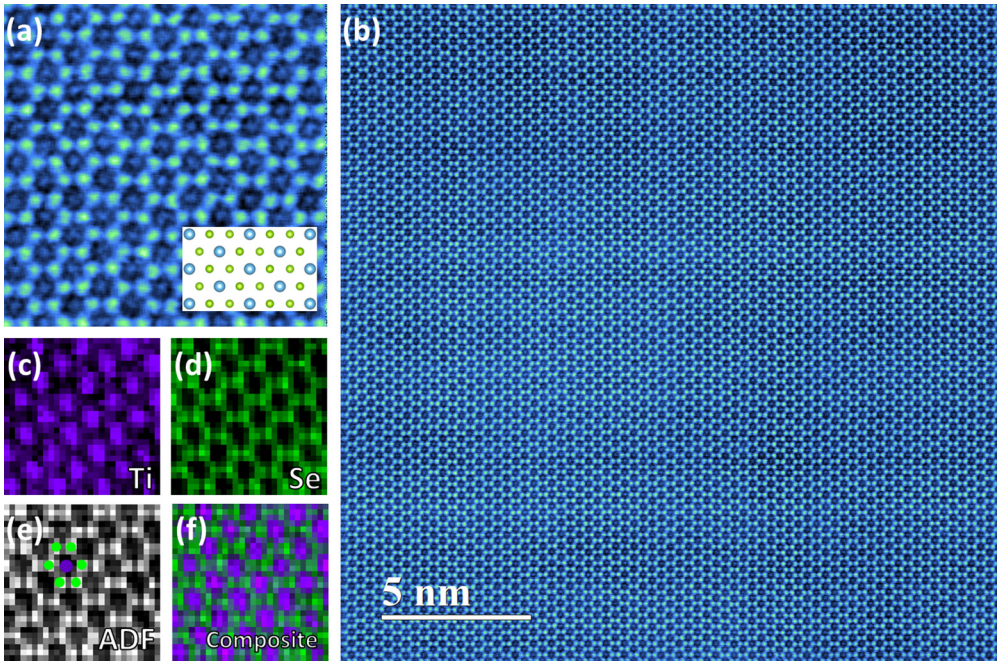

FIG. 1. (a) False color HAADF-STEM image of $1T$-$TiSe_2$, where Ti atoms are blue and Se atoms are green. Inset: Atomic model showing the same atomic structure of $1T$-$TiSe_2$. (b) HAADF-STEM image of $1T$-$TiSe_2$ taken at relatively low magnification showing that the sample is free of dislocations and planar defects. (c)–(f) EELS elemental mapping of $1T$-$TiSe_2$ showing atomic-resolution signals from (c) Ti $L_{3,2}$ edge, (d) Se $M_{2,3}$ edge, (e) simultaneously acquired ADF image, and (f) composite image of Ti and Se.

in-plane and out-of-plane coherence lengths. First-principles density functional theory (DFT) calculations are integrated to explore the electronic feature of CDW in $1T$-$TiSe_2$.

II. METHODS

We used the aberration-corrected JEOL JEM-ARM200CF STEM to acquire high angle annular dark field (HAADF) images, EELS, and PACBED. The microscope was operated at 80 keV. The convergence angle used for STEM/EELS acquisition was 24–27 mrad and for PACBED it was 8–9 mrad. We used JEOL JEM-2100F to perform coherent NED studies. By using a 10 μm condenser aperture, the electron probe size can be confined to $\sim$50 nm. A liquid helium cooling stage was used for EELS and PACBED acquisition at 19 and 28 K, respectively. A liquid nitrogen cooling stage was used for the NED study at 89 K. DFT calculations were performed using the Vienna *ab initio* simulation package (VASP) with a plane-wave basis set [24,25] and the projector augmented wave method [26]. The semilocal metageneralized gradient approximation with a Perdew-Burke-Ernzerhof functional was employed to treat the exchange-correlation effect [27,28]. The kinetic energy cutoff was set to 420 eV. A Γ-centered k-point mesh up to $21 \times 21 \times 13$ was used in the density of states (DOS) calculations. The structure of $1T$ and the CDW phase was fully relaxed until the force on each ion was less than 0.01 eV/Å.

III. RESULTS AND DISCUSSION

Figure 1(a) shows an atomic-resolution STEM HAADF image of $1T$-$TiSe_2$ viewing from its [001] direction at room temperature. The contrast of the image is proportional to the atomic number, therefore Se atoms appear to be brighter than Ti. The inserted model indicates that one Ti atom (blue) is surrounded by six Se atoms (green), three of which are above the Ti layer and three below, forming the space group of $P\bar{3}m1$. A lower magnification image shows that the flake is free of dislocations and planar defects [Fig. 1(b)], confirming the long-range order of the $1T$ phase. Figures 1(c)–1(f) form a set of atomic-resolution EELS elemental mappings that matches the atomic structure obtained by the ADF image. Ti and Se atomic columns are mapped using energy-loss signals from the Ti $L_{3,2}$ edge and Se $M_{2,3}$ edge, respectively.

Direct evidence of a CDW phase can be obtained from electron diffraction, in which the $2 \times 2 \times 2$ superlattice generates $(1/2, 1/2, 1/2)$ Bragg peaks. Coherent NED was utilized to perform the study of the structural modulation. NED is generated by a coherent parallel electron beam, and has a much smaller probe size compared to conventional selected area electron diffraction (SAED) [29]. The diffraction pattern of NED looks similar to that of SAED, but is more adequate for a quantitative study of nanostructures given its smaller probe size and abundant phase information. To confirm the existence of CDW, we acquired NED on $1T$-$TiSe_2$ using a liquid nitrogen cooling stage at 89 K. Figure 2 shows a comparison between NED patterns taken before [Fig. 2(a)] and after [Fig. 2(b)] *in situ* liquid nitrogen cooling. At 89 K, we find clear evidence of a $2 \times 2 \times 2$ superlattice between the zero-order Laue zone (ZOLZ) and the first-order Laue zone (FOLZ), which is generated by the commensurate CDW phase.

For the commensurate CDW phase of $1T$-$TiSe_2$—a well-known triple-$\boldsymbol{q}$ system—the CDW wave vectors $\boldsymbol{q}_i$ ($i = 1,2,3$) are expressed as a linear combination of the reciprocal lattice vectors $\boldsymbol{a}_i^*$ such that $\boldsymbol{q}_1 = \frac{1}{2}(\boldsymbol{a}_1^* + \boldsymbol{a}_3^*)$, while $\boldsymbol{q}_2$ and $\boldsymbol{q}_3$ can be obtained by rotating $\boldsymbol{q}_1$ around the $\boldsymbol{a}_3^*$ direction by $\pm 120^\circ$. For most triple-$\boldsymbol{q}$ CDW systems such as $1T$-TaS_2 and

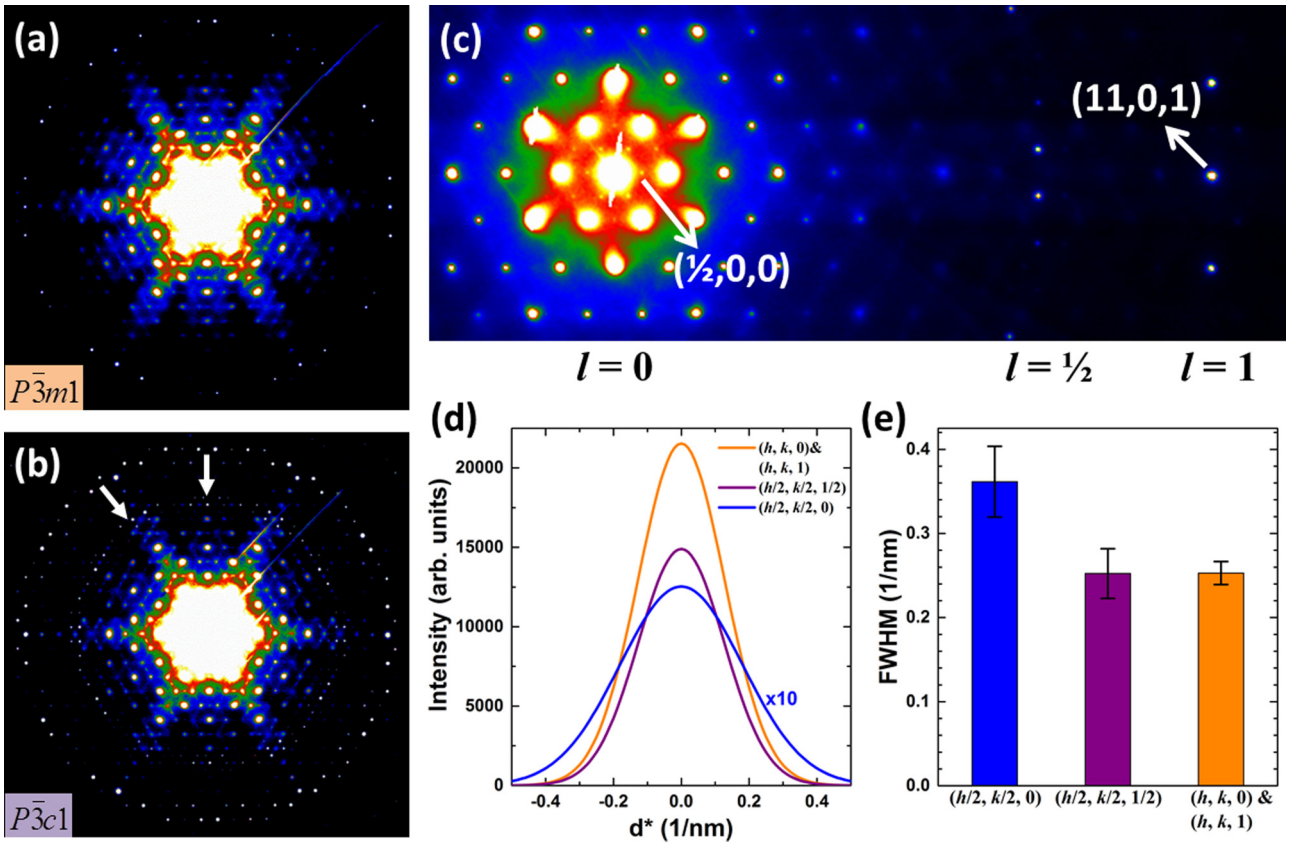

FIG. 2. (a) NED pattern acquired at room temperature including FOLZ showing the $P\bar{3}m1$ space group. (b) NED pattern acquired at 89 K including FOLZ showing the $P\bar{3}c1$ space group, with $(1/2,1/2,1/2)$ Bragg peaks emerging between ZOLZ and FOLZ. (c) NED pattern cropped from (b) with reduced intensity saturation of the ZOLZ, showing Bragg peaks corresponding to the superlattice in ZOLZ ($l = 0$) and the CDW ring ($l = 1/2$). (d) Gaussian fitting of the in-plane CDW $(h/2,k/2,0)$ peaks (blue), out-of-plane CDW $(h/2,k/2,1/2)$ peaks (purple), and fundamental structure $(h,k,0)$ and $(h,k,1)$ peaks (orange). The intensity of the blue curve has been enlarged ten times for visual convenience. (e) FWHM measurement of the in-plane CDW $(h/2,k/2,0)$ peaks, out-of-plane CDW $(h/2,k/2,1/2)$ peaks, and fundamental structure $(h,k,0)$ and $(h,k,1)$ peaks.

$2H$-$TaSe_2$, the CDW wave vectors consist of only in-plane components [30], therefore, in reciprocal space, the CDW Bragg peaks only emerge in the Laue zones where the order numbers are integers (zero order, first order, etc.). In $1T$-$TiSe_2$, however, given the out-of-plane component, extra Bragg peaks emerge between the zero-order and first-order Laue zones. This system appears to be an ideal case to study the in-plane and out-of-plane coherence of CDW.

The NED pattern we acquired at a cryogenic temperature consists of three portions: the zero-order Laue zone consisting of $(h,k,0)$ and $(h/2,k/2,0)$ Bragg peaks in the center that contains in-plane structural information, the first-order Laue zone consisting of $(h,k,1)$ Bragg peaks as the outmost ring that contains out-of-plane structural information, and the $(h/2,k/2,1/2)$ Bragg peaks that form a ring between the zero-order and first-order Laue zones, carrying out-of-plane CDW structural information, as illustrated in Fig. 2(c). The diffraction spots, on the other hand, consist of two categories: fundamental spots (h,k,l) that come from the original $1 \times 1 \times 1$ structure, and CDW spots $(h/2,k/2,0)$ and $(h/2,k/2,1/2)$ generated by the superlattice. For samples with a finite thickness, the reciprocal lattice is a three-dimensional (3D) array of relrods, and the real space structure and geometry associated with them determines the shape of the relrods. A rational assumption we adopted is that the shape of the original $1 \times 1 \times 1$ structure can be approximated by an infinitely large disk, but due to the beam size ($\sim$50 nm) confinement, the sampling volume is $\pi \times 50^2 \times c\,\mathrm{nm}^3$, where c is the sample thickness, hence the relrods associated with the isotropic, long-range coherent fundamental structure take the shape of a near sphere; if the $2 \times 2 \times 2$ superlattice forms certain domains instead of an infinitely large disk, the shape of the relrods changes accordingly and can be measured from the diffraction pattern. The mean domain size can be estimated using the Debye-Scherrer equation

$$D = \frac{k\lambda}{\beta \cos\theta},$$

where k is the shape factor with values between 0.9 and 1 depending on the shape of the domain, λ is the electron wavelength (2.5 pm for a 200 keV electron probe), β is the full width at half maximum (FWHM) of the Bragg peaks, and θ is the Bragg angle. In our NED pattern, for the innermost Bragg peak (1/2,0,0), the Bragg angle is 2.042 mrad; for the outermost Bragg peak (11,0,1), the Bragg angle is 44.873 mrad. The value of $\cos\theta$ therefore varies from 1 to 0.999, and can be neglected in this equation. The domain size eventually becomes inversely proportional to the FWHM of the Bragg peaks.

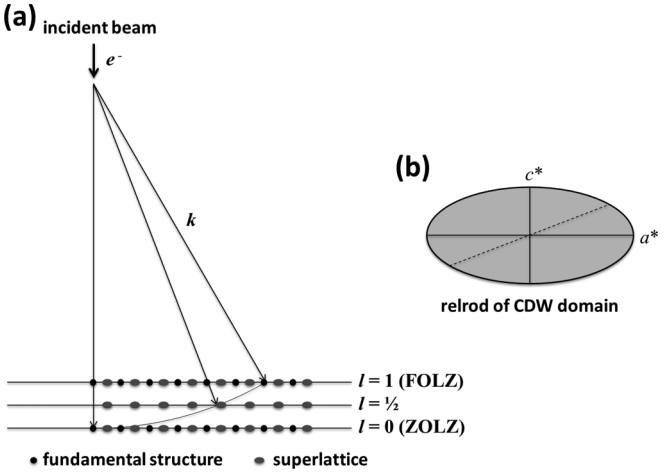

FIG. 3. (a) Schematic showing how the Ewald sphere cuts the relrods in reciprocal space. (b) Schematic showing the elliptical relrod of a cylindrically shaped CDW domain.

We therefore extract the Bragg peaks of in-plane CDW spots $(h/2,k/2,0)$ and out-of-plane CDW spots $(h/2,k/2,1/2)$, and compare them with the fundamental spots $(h,k,0)$ and $(h,k,1)$. We fit the peaks with a Gaussian function and the results are shown in Fig. 2(d). The FWHM of the peaks are measured to be $0.36 \pm 0.041/\text{nm}$ for $(h/2,k/2,0)$, $0.25 \pm 0.031/\text{nm}$ for $(h/2,k/2,1/2)$, and $0.25 \pm 0.011/\text{nm}$ for $(h,k,0)$ and $(h,k,1)$, respectively. The width of a diffraction spot depends on how the Ewald sphere is cutting the relrod, as shown in Fig. 3(a). The shape of the relrod depends on the real space geometry of the sample. For the fundamental $1 \times 1 \times 1$ structure, the sample is infinitely large in plane, but the beam size confines the sampling area to a circle with a diameter of $\sim$50 nm; the out-of-plane size is confined by the sample thickness, hence the corresponding relrod is a near sphere given that the sample thickness is around 30–50 nm. Therefore, for fundamental spots, the FWHM does not change significantly between ZOLZ and FOLZ given their spherical shape, as also verified by our measurement [the orange bar with the smallest standard deviation in Fig. 2(e)].

For the CDW superlattice, the in-plane spots $(h/2,k/2,0)$ have a significant broadening compared to the out-of-plane spots $(h/2,k/2,1/2)$, but the out-of-plane spots are nearly identical to the fundamental spots. To explain the likely scenario, we build the schematic shown in Fig. 3(b). For an elliptically shaped relrod, its width a^* is much larger than its height c^*, while the height is confined by the sample thickness. When the Ewald sphere cuts the CDW relrod in the ZOLZ, the width we get is a^*. When the Ewald sphere cuts the CDW relrod in the $l = 1/2$ plane, the width decreases significantly, as shown by the dashed line in the schematic. In this case, the real space shape of CDW domain corresponding to the elliptically shaped relrod would have a short in-plane dimension and a long out-of-plane dimension confined by sample thickness, therefore we predict that the CDW domain has a cylindrical shape. Of course, we are aware that the width of the diffraction spots is also affected by the projection angle since the CCD is flat. However, we have measured the lattice constants in both ZOLZ and FOLZ, and found no difference between the two. We are convinced that the projection angle-induced distortion can be considered as a secondary effect that has a minor or negligible contribution to the change of FWHM, given the primary effect caused by the relrod shape change is significantly larger.

By quantitatively analyzing the NED pattern, we have derived that in $1T$-$TiSe_2$, the CDW domains form a cylindrical

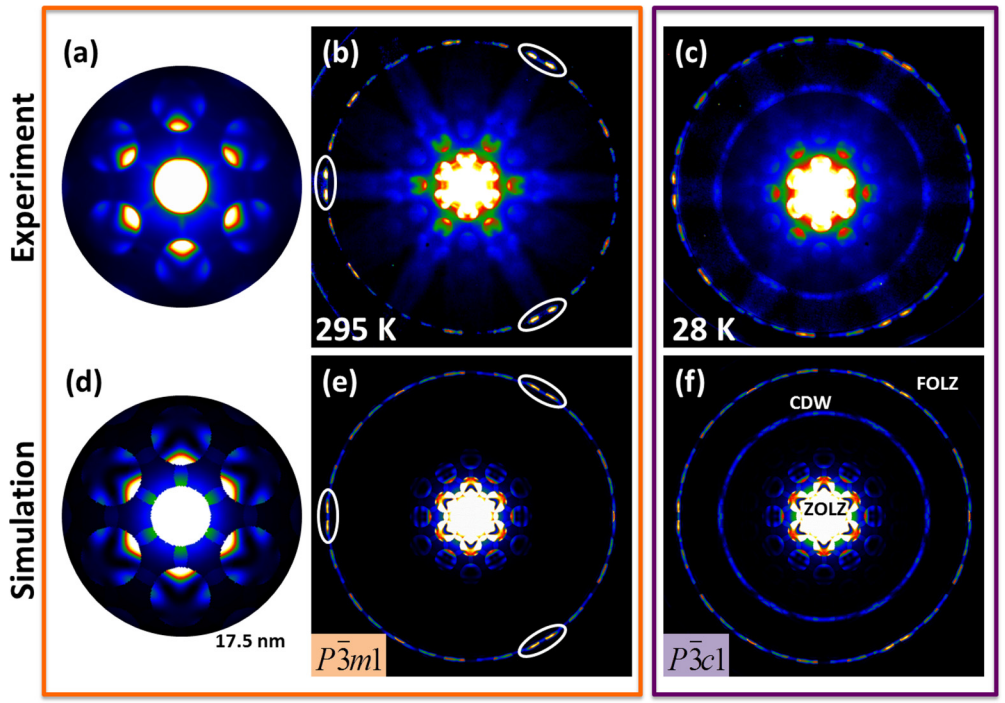

FIG. 4. CBED patterns showing (a) ZOLZ at room temperature. (b) FOLZ lines at room temperature, where white ovals indicate the structure symmetry is threefold instead of sixfold. (c) FOLZ and CDW lines at 28 K. (d)–(f) Bloch-wave-based simulations of (a)–(c), respectively.

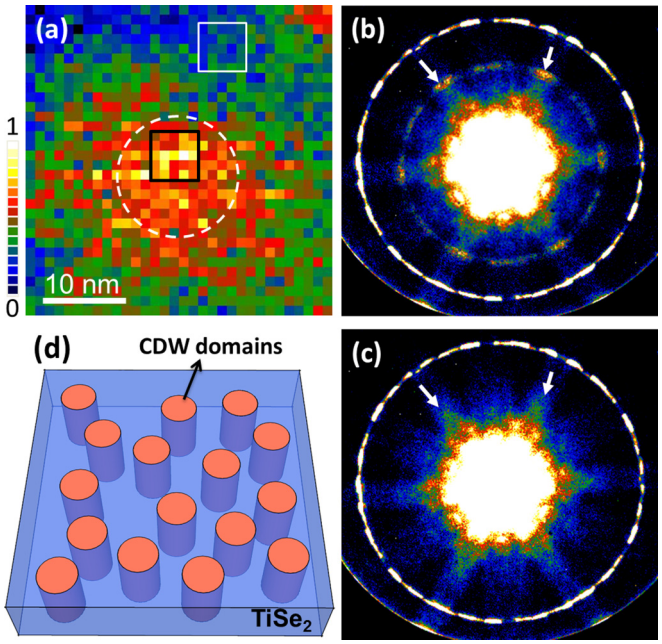

FIG. 5. (a) Real space mapping of the CDW line intensity, showing a domain structure of ∼10 nm. CBED patterns are extracted from the black and white squares, as shown in (b) and (c), respectively. (b) CBED pattern showing a visible CDW line, indicating a $2 \times 2 \times 2$ superlattice in this area. (c) CBED patterns showing no CDW line, indicating the original $1 \times 1 \times 1$ structure in this area. The color bar has an arbitrary unit. (d) Schematic showing cylindrically shaped CDW domains randomly distributed in the $TiSe_2$ slab.

shape; their in-plane coherence length is short, but the out-of-plane coherence length is long. To date, there is no direct evidence from real space that can validate our observation, hence an *in situ* position-averaged CBED at a cryogenic temperature is utilized to perform a three-dimensional investigation.

In order to study the CDW domain structure in real space, we acquired position-averaged CBED on the $1T$-$TiSe_2$ flake at both room temperature (295 K) and a cryogenic temperature (28 K). In a PACBED mapping, the convergent electron probe scans an area in a raster while recording the CBED pattern at each pixel [31]. Therefore, local structural information can be extracted from the mapping, and nanometer-sized domains with different structural properties become visible [32]. Combined with Bloch-wave-based simulations, PACBED can also be used to accurately measure the sample thickness. Figure 4 illustrates how PACBED is used for a thickness measurement and phase transition study. Figures 4(a)–4(c) are experimental CBED patterns, and Figs. 4(d)–4(f) are simulation results. Figure 4(a) is a CBED pattern from the ZOLZ; simulations were carried out [Fig. 4(d)], and the thickness of this area was found to be 17.5 nm. Compared to the sixfold symmetry in ZOLZ, FOLZ lines provide much more accurate symmetry information since they include out-of-plane wave vectors, so we can see the threefold symmetry of $1T$-$TiSe_2$, as indicated by the white ovals in Figs. 4(b) and 4(e). Shown in Fig. 4(c), after *in situ* cooling to 28 K, we found additional lines between ZOLZ and FOLZ lines that correspond to the $2 \times 2 \times 2$ CDW superlattice, but the structural parameter change is so small that the FOLZ lines are nearly identical to those at room temperature. Simulated CBED patterns in Figs. 4(e) and 4(f) are in good agreement with experiment, confirming the existence of a CDW phase.

We extract CBED patterns from each pixel of the PACBED mapping. In a CBED pattern, by selecting only the CDW lines, we inversely map their intensity distribution back to real space. Figure 5(a) shows a mapping of the CDW signal intensity, showing a stark contrast between the CDW maxima [Fig. 5(b)] and minima [Fig. 5(c)], and the CDW maxima form a domain of ∼10 nm. Within this domain, the CDW signal is strong and uniform, indicating that the long-range coherence of the out-of-plane component is preserved. Combining PACBED mapping with the NED pattern, we conclude that a typical CDW domain forms a cylindrical shape, with an in-plane coherence length of ∼10 nm and out-of-plane coherence length with a 17.5 nm lower bound, as illustrated in Fig. 5(d).

Upon the CDW phase transition, a structural modulation takes place and lowers the symmetry of the system from $P\bar{3}m1$ to $P\bar{3}c1$. The upper and lower layers of Se atoms surrounding Ti rotate in opposite directions, rendering a change in coordination from an octahedron towards a trigonal prismatic [6], hence the electronic structure changes. In transition metal dichalcogenite systems, the lowest conduction bands are constituted of metal d bands, herein the Ti $3d$ band. In the case of $1T$-$TiSe_2$, the Ti $3d$ band splits into

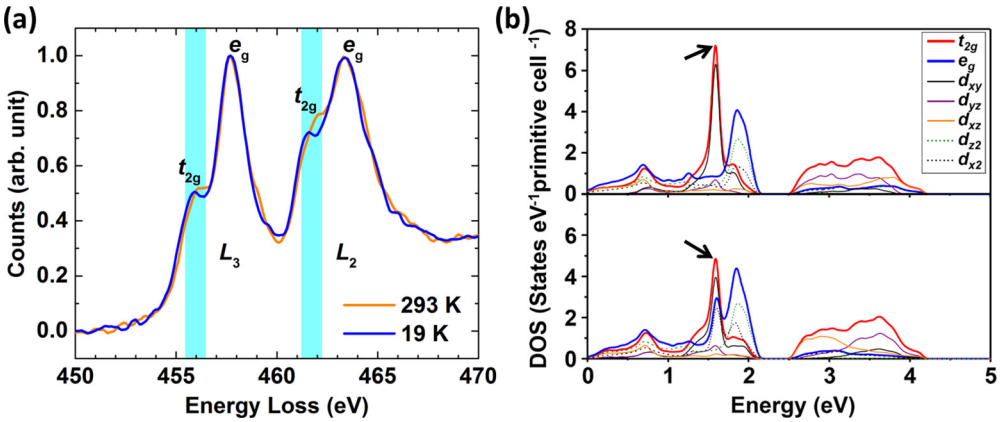

FIG. 6. (a) EEL spectra of Ti $L_{3,2}$ edge acquired at room temperature (orange) and 19 K (blue), showing the difference in the t_{2g} intensity. (b) DFT calculation of Ti DOS of the t_{2g} and e_g orbitals, showing a decrease in the t_{2g} peak above the Fermi level due to a CDW phase transition.

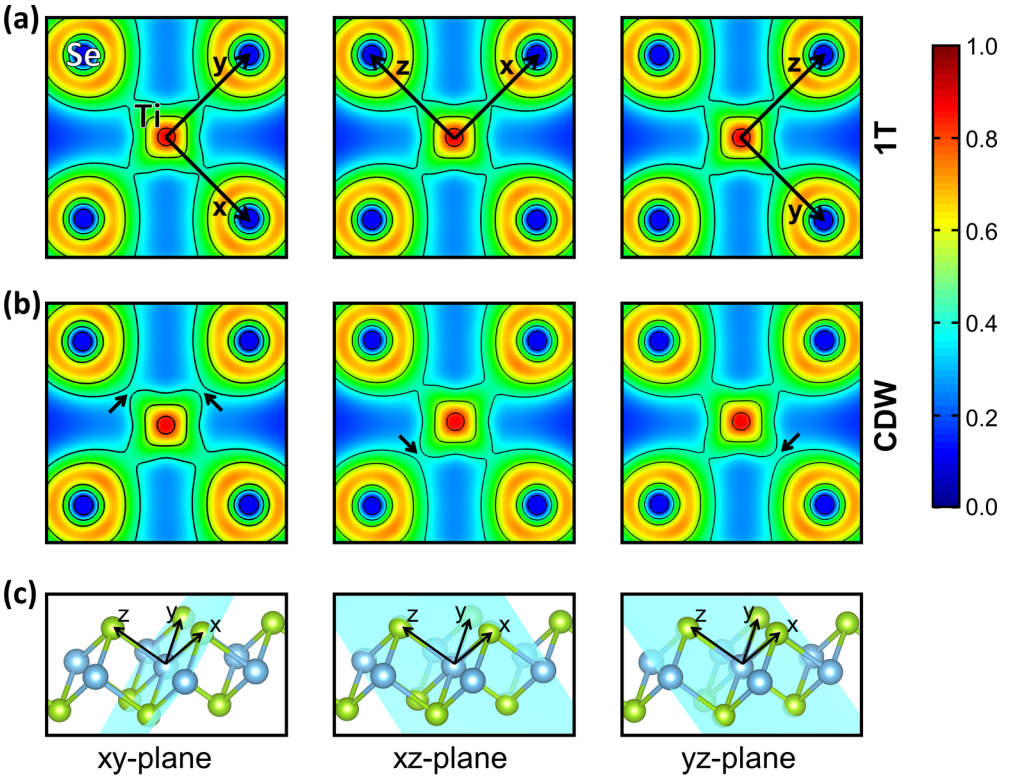

FIG. 7. (a) First-principles prediction of the valence charge density map of a Ti-Se plane in $1T$-$TiSe_2$ showing twofold symmetry. In this plane, one Ti atom in the center (red) is surrounded by four Se atoms in the corner (blue). (b) Valence charge density mapping of the same Ti-Se plane in the CDW phase showing symmetry breaking along the Ti-Se bond direction. The color bar shows a charge density from 0 to 1 $eV/Å^3$. (c) Atomic model showing the Ti-Se xy, xz, and yz planes where the valence charge density is mapped.

lower-energy t_{2g} orbitals and higher-energy e_g orbitals [30,33]; the t_{2g} orbitals cross the Fermi level at the L point and form an electron pocket, therefore the CDW phase transition mainly affects the t_{2g} orbitals. We acquired EELS spectra of Ti L edge at 293 K ($1T$ phase) and 19 K (CDW phase) and observed changes in the electronic structural modulation. As shown in Fig. 6(a), at cryogenic temperatures, the t_{2g}-e_g splitting in both the L_3 and L_2 edges enlarges, the intensities of the t_{2g} peaks decrease significantly, and the low-energy side of the e_g peak broadens, causing a redshift of the t_{2g}-e_g splitting. Such changes indicate that the hybridization of Ti $3d$ and Se $4p$ has changed significantly upon CDW formation, as CDW-induced band backfolding would result in an increase of occupied states in the t_{2g} orbitals below the Fermi surface, and, equivalently, a decrease of unoccupied states in the t_{2g} orbitals further up. DFT calculations further confirmed that the CDW phase transition is accompanied by changes to the Ti $3d$ orbitals. Figure 6(b) displays the density of states of the Ti $3d$ band in both the $1T$ and CDW phases above the Fermi level. From $1T$ to CDW, we notice a significant decrease in the t_{2g} orbital, which stems from the decrease of the d_{xy} orbital; an additional peak emerges in the e_g orbital, which originates from the increase of the d_{x^2} orbital. It is worth noticing, however, that DFT only calculates the charge orbitals in the ground state, while EELS probes the transition from lower occupied core states to higher unoccupied states. Nevertheless, EELS and DOS results agree with each other qualitatively very well as the change in the final states would always affect the transition from the initial states.

Given the quasi-two-dimensional nature of $1T$-$TiSe_2$, anisotropy at the atomic level is not unexpected. Studies have also shown macroscopic anisotropy by measuring the in-plane and out-of-plane resistivity [1]. Our direct observation of nanometer-sized cylindrically shaped CDW domains, however, indicates anisotropy at the nanoscale. Since the atomic position and atomic displacements in the CDW phase are known, it is straightforward to calculate the valence charge density of $1T$-$TiSe_2$ in both the $1T$ and CDW phases. In Fig. 7(a), we plot the valence charge density of $1T$-$TiSe_2$ from a Ti-Se plane that cuts through the two top layers of Se, one middle layer of Ti, and two bottom layers of Se, as illustrated in Fig. 7(c). In this plane, Ti and Se form pd-hybridized bonds, hence CDW/PLD would greatly affect the bonding configuration. As shown in Fig. 7(a), the charge density map of the $1T$ phase shows a twofold symmetry; in the CDW phase, the twofold symmetry is broken due to the displacement of Ti and Se atoms, as shown in Fig. 7(b). In Fig. 7, we plot the charge density map on the xy, xz, and yz planes, and clearly observe a difference in bond shape between these planes. It is worth noticing that the symmetry breaking here takes place in a single Ti-Se octahedron, and threefold in-plane symmetry is still preserved when a $2 \times 2 \times 2$ supercell is considered. These results agree very well with the previous studies in Ref. [1], and are presented here to provide a detailed picture of how the bonding configuration changes during the CDW phase transition. Many opportunities still exist for studying the electronic origin of the anisotropic CDW domain, which

could be driven by anisotropic electron-phonon coupling and/or anisotropic electron-electron interactions. Such efforts could benefit from a further understanding of how the local electronic structure evolves.

According to the BCS theory, electron-phonon coupling could drive the formation of electron pairs that leads to conventional superconductivity; electron-phonon coupling determines the critical temperature T_c, and the critical field is a function of T/T_c [34]. The discovery of anisotropic properties in Cu-intercalated $1T$-$TiSe_2$ implies that the electron-phonon interaction is anisotropic in the superconducting state [35]. Such anisotropy has also been observed in $NbSe_2$ [36–38]. The relationship between the CDW state and superconducting state has been a long-standing mystery that still needs to be elucidated. It is widely accepted that CDW and superconducting are competing orders and suppress each other, and CDW often emerges above the superconducting dome in the phase diagrams [12–14,39–41]. Theoretical studies have reproduced the pressure phase diagram with competing CDW and superconducting orders, as well as a superconducting dome, in the framework of electron-phonon coupling without excitonic effects, suggesting that the connection between CDW and superconducting is dominated by electron-phonon coupling [42]. For both Cu-intercalation and pressure-induced superconductivity formation, CDW domain walls are found to be the triggering factor [13,43]. Our study showed, in the CDW regime, the anisotropy of in-plane and out-of-plane CDW in $1T$-$TiSe_2$. Based on the McMillan model, a short in-plane coherence length suggests strong electron-phonon coupling, while a long out-of-plane coherence length suggests relatively weak coupling [44]. Our discovery of anisotropic CDW domains could shed light on understanding the emergence of superconductivity in three dimensions. Moreover, many physical properties in CDW phase transitions, such as transition temperature and resistivity, are altered with reduced dimensionality, meaning the out-of-plane coherence could also be used to tune these parameters [45].

IV. SUMMARY

In summary, combining atomically resolved STEM imaging, diffraction, and EELS, we have studied the atomic structure and electronic structure of $1T$-$TiSe_2$. In the CDW state, the NED patterns revealed the three-dimensional nature of CDW coherence, suggesting in-plane and out-of-plane anisotropy. In addition to the periodic lattice distortion observed with electron diffraction, we studied charge modulation using EELS, revealing that electron modulation and lattice modulation take place simultaneously. Supported by DFT calculations, EELS could confirm the CDW state with a high spatial resolution, and serve as a step toward the characterization of the electronic structure change at the domain boundaries with atomic resolutions. Our unique integrated approach to investigate the three-dimensional nature of the CDW domain can serve as guidance for future atomically resolved studies in two-dimensional systems when an out-of-plane phenomenon is of interest, and for convenient extraction of three-dimensional information by a quantitative analysis of electron diffraction. It can be further used to correlate, for example, CDW and superconductivity, as well as to understand emerging behavior in thin films due to the reduced dimensionality.

ACKNOWLEDGMENTS

This work was supported as part of the Center for the Computational Design of Functional Layered Materials, an Energy Frontier Research Center funded by the U.S. Department of Energy, Office of Science, Basic Energy Sciences under Award No. DE-SC0012575 (TEM and DFT studies). J.T., L.W., Y.Z., and the electron microscopy facility involved in this work at BNL were supported by the Materials Science and Engineering Divisions, Office of Basic Energy Sciences of the U.S. Department of Energy under Contract No. DE-SC0012704 (TEM data analysis). J.-C.Z. was supported by the National Natural Science Foundation of China under Award No. 11335006 (DFT data analysis).

[1] F. J. Di Salvo, D. E. Moncton, and J. V. Waszczak, Phys. Rev. B **14**, 4321 (1976).
[2] M. D. Johannes and I. I. Mazin, Phys. Rev. B **77**, 165135 (2008).
[3] H. Cercellier, C. Monney, F. Clerc, C. Battaglia, L. Despont, M. G. Garnier, H. Beck, P. Aebi, L. Patthey, H. Berger, and L. Forro, Phys. Rev. Lett. **99**, 146403 (2007).
[4] M. M. May, C. Brabetz, C. Janowitz, and R. Manzke, Phys. Rev. Lett. **107**, 176405 (2011).
[5] G. Monney, C. Monney, B. Hildebrand, P. Aebi, and H. Beck, Phys. Rev. Lett. **114**, 086402 (2015).
[6] H. P. Hughes, J. Phys. C: Solid State **10**, L319 (1977).
[7] M. Holt, P. Zschack, H. Hong, M. Y. Chou, and T. C. Chiang, Phys. Rev. Lett. **86**, 3799 (2001).
[8] K. Rossnagel, L. Kipp, and M. Skibowski, Phys. Rev. B **65**, 235101 (2002).
[9] M. Porer, U. Leierseder, J. M. Menard, H. Dachraoui, L. Mouchliadis, I. E. Perakis, U. Heinzmann, J. Demsar, K. Rossnagel, and R. Huber, Nat. Mater. **13**, 857 (2014).
[10] C. Monney, M. Puppin, C. W. Nicholson, M. Hoesch, R. T. Chapman, E. Springate, H. Berger, A. Magrez, C. Cacho, R. Ernstorfer, and M. Wolf, Phys. Rev. B **94**, 165165 (2016).
[11] A. Kogar, S. Vig, M. S. Rak, A. A. Husain, F. Flicker, Y. I. Joe, L. Venema, G. J. MacDougall, T. C. Chiang, E. Fradkin, J. van Wezel, and P. Abbamonte, arXiv:1611.04217.
[12] A. F. Kusmartseva, B. Sipos, H. Berger, L. Forro, and E. Tutis, Phys. Rev. Lett. **103**, 236401 (2009).
[13] Y. I. Joe, X. M. Chen, P. Ghaemi, K. D. Finkelstein, G. A. de la Peña, Y. Gan, J. C. T. Lee, S. Yuan, J. Geck, G. J. MacDougall, T. C. Chiang, S. L. Cooper, E. Fradkin, and P. Abbamonte, Nat. Phys. **10**, 421 (2014).
[14] E. Morosan, H. W. Zandbergen, B. S. Dennis, J. W. G. Bos, Y. Onose, T. Klimczuk, A. P. Ramirez, N. P. Ong, and R. J. Cava, Nat. Phys. **2**, 544 (2006).
[15] F. Weber, S. Rosenkranz, J. P. Castellan, R. Osborn, G. Karapetrov, R. Hott, R. Heid, K. P. Bohnen, and A. Alatas, Phys. Rev. Lett. **107**, 266401 (2011).
[16] M. Iavarone, R. Di Capua, X. Zhang, M. Golalikhani, S. A. Moore, and G. Karapetrov, Phys. Rev. B **85**, 155103 (2012).

[17] J.-P. Peng, J.-Q. Guan, H.-M. Zhang, C.-L. Song, L. Wang, K. He, Q.-K. Xue, and X.-C. Ma, Phys. Rev. B **91**, 121113 (2015).
[18] B. Hildebrand, T. Jaouen, C. Didiot, E. Razzoli, G. Monney, M. L. Mottas, A. Ubaldini, H. Berger, C. Barreteau, H. Beck, D. R. Bowler, and P. Aebi, Phys. Rev. B **93**, 125140 (2016).
[19] D. Qian, D. Hsieh, L. Wray, E. Morosan, N. L. Wang, Y. Xia, R. J. Cava, and M. Z. Hasan, Phys. Rev. Lett. **98**, 117007 (2007).
[20] P. Chen, Y. H. Chan, X. Y. Fang, Y. Zhang, M. Y. Chou, S. K. Mo, Z. Hussain, A. V. Fedorov, and T. C. Chiang, Nat. Commun. **6**, 8943 (2015).
[21] K. Sugawara, Y. Nakata, R. Shimizu, P. Han, T. Hitosugi, T. Sato, and T. Takahashi, ACS Nano **10**, 1341 (2016).
[22] A. H. Moudden, J. D. Axe, P. Monceau, and F. Levy, Phys. Rev. Lett. **65**, 223 (1990).
[23] E. Sweetland, C. Y. Tsai, B. A. Wintner, J. D. Brock, and R. E. Thorne, Phys. Rev. Lett. **65**, 3165 (1990).
[24] G. Kresse and J. Furthmuller, Phys. Rev. B **54**, 11169 (1996).
[25] G. Kresse and J. Furthmuller, Comput. Mater. Sci. **6**, 15 (1996).
[26] P. E. Blöchl, Phys. Rev. B **50**, 17953 (1994).
[27] J. P. Perdew, K. Burke, and M. Ernzerhof, Phys. Rev. Lett. **77**, 3865 (1996).
[28] J. Sun, B. Xiao, Y. Fang, R. Haunschild, P. Hao, A. Ruzsinszky, G. I. Csonka, G. E. Scuseria, and J. P. Perdew, Phys. Rev. Lett. **111**, 106401 (2013).
[29] J. M. Zuo, M. Gao, J. Tao, B. Q. Li, R. Twesten, and I. Petrov, Microsc. Res. Tech. **64**, 347 (2004).
[30] K. Rossnagel, J. Phys.: Condens. Matter **23**, 213001 (2011).
[31] J. M. Lebeau, S. D. Findlay, L. J. Allen, and S. Stemmer, Ultramicroscopy **110**, 118 (2010).
[32] J. Tao, D. Niebieskikwiat, M. Varela, W. Luo, M. A. Schofield, Y. Zhu, M. B. Salamon, J. M. Zuo, S. T. Pantelides, and S. J. Pennycook, Phys. Rev. Lett. **103**, 097202 (2009).
[33] J. van Wezel, P. Nahai-Williamson, and S. S. Saxena, Phys. Rev. B **81**, 165109 (2010).
[34] J. Bardeen, L. N. Cooper, and J. R. Schrieffer, Phys. Rev. **108**, 1175 (1957).
[35] E. Morosan, L. Li, N. P. Ong, and R. J. Cava, Phys. Rev. B **75**, 104505 (2007).
[36] P. de Trey, S. Gygax, and J.-P. Jan, J. Low Temp. Phys. **11**, 421 (1973).
[37] D. Sanchez, A. Junod, J. Muller, H. Berger, and F. Lévy, Physica B: Condens. Matter **204**, 167 (1995).
[38] T. Valla, A. V. Fedorov, P. D. Johnson, P. A. Glans, C. McGuinness, K. E. Smith, E. Y. Andrei, and H. Berger, Phys. Rev. Lett. **92**, 086401 (2004).
[39] R. Sooryakumar and M. V. Klein, Phys. Rev. Lett. **45**, 660 (1980).
[40] A. H. Castro Neto, Phys. Rev. Lett. **86**, 4382 (2001).
[41] J. Chang, E. Blackburn, A. T. Holmes, N. B. Christensen, J. Larsen, J. Mesot, R. Liang, D. A. Bonn, W. N. Hardy, A. Watenphul, M. v. Zimmermann, E. M. Forgan, and S. M. Hayden, Nat. Phys. **8**, 871 (2012).
[42] M. Calandra and F. Mauri, Phys. Rev. Lett. **106**, 196406 (2011).
[43] S. Yan, D. Iaia, E. Morosan, E. Fradkin, P. Abbamonte, and V. Madhavan, Phys. Rev. Lett. **118**, 106405 (2017).
[44] W. L. McMillan, Phys. Rev. B **16**, 643 (1977).
[45] D. L. Duong, G. Ryu, A. Hoyer, C. Lin, M. Burghard, and K. Kern, ACS Nano **11**, 1034 (2017).